Check for updates

ADVANCING EARTH AND SPACE SCIENCES

Geophysical Research Letters

RESEARCH LETTER
10.1029/2023GL102960

High Spatial Melt Rate Variability Near the Totten Glacier Grounding Zone Explained by New Bathymetry Inversion

Irena Vaňková[1,2], J. Paul Winberry[3], Sue Cook[4], Keith W. Nicholls[2], Chad A. Greene[5], and Benjamin K. Galton-Fenzi[4,6]

[1]Los Alamos National Laboratory, Los Alamos, NM, USA, [2]British Antarctic Survey, Natural Environment Research Council, Cambridge, UK, [3]Department of Geological Sciences, Central Washington University, Ellensburg, WA, USA, [4]Australian Antarctic Program Partnership, Institute for Marine and Antarctic Studies, University of Tasmania, Hobart, TAS, Australia, [5]Jet Propulsion Laboratory, California Institute of Technology, Pasadena, CA, USA, [6]Australian Antarctic Division, Kingston, TAS, Australia

Key Points:

- Totten Glacier melt rates vary spatially between 0 and over 20 m/a; differences are explained by water column thickness variations from updated bathymetry
- Temporal melt rate variability is primarily inter-annual; melt rates differ by 7–9 m/a over two observed years and there is no clear seasonal cycle
- Contrary to previous findings, we find no topographic barriers to the intrusion of warm water to the Totten Glacier grounding zone

Supporting Information:

Supporting Information may be found in the online version of this article.

Correspondence to:

I. Vaňková,
vankova@lanl.gov

Citation:

Vaňková, I., Winberry, J. P., Cook, S., Nicholls, K. W., Greene, C. A., & Galton-Fenzi, B. K. (2023). High spatial melt rate variability near the Totten Glacier grounding zone explained by new bathymetry inversion. *Geophysical Research Letters*, *50*, e2023GL102960. https://doi.org/10.1029/2023GL102960

Received 20 JAN 2023
Accepted 8 MAY 2023

© 2023. The Authors.
This is an open access article under the terms of the Creative Commons Attribution License, which permits use, distribution and reproduction in any medium, provided the original work is properly cited.

Abstract

Totten Glacier is a fast-moving East Antarctic outlet with the potential for significant future sea-level contributions. We deployed four autonomous phase-sensitive radars on its ice shelf to monitor ice-ocean interactions near its grounding zone and made active source seismic observations to constrain gravity-derived bathymetry models. We observe an asymmetry in basal melting with mean melt rates along the grounding zone differing by up to 20 m/a. Our new bathymetry model reveals that this melt rate asymmetry coincides with an asymmetry in water column thickness and that the low-melting ice-shelf portion is shielded from the main cavity circulation. A 2-year record yields year-to-year melt rate variability of 7–9 m/a with no seasonal cycle. Our results highlight the key role of bathymetry near grounding lines for accurate modeling of ice-shelf melt, and the importance of sustained multi-year monitoring, especially at ice-shelf cavities where the dominant melt rate drivers vary primarily inter-annually.

Plain Language Summary

The point were the Antarctic Ice Sheet goes afloat on the ocean represents a critical region, where minor variations in melt rates can impact glacier flow and influence the rate of sea-level rise. East Antarctica's Totten Glacier holds the potential to raise global sea level by several meters. Therefore, to understand the conditions it is exposed to, we measured melt rates for 2 years in several key locations near the point where the ice first touches the ocean. Our new measurements of the shape of the Totten Ice Shelf cavity help explain an observed spatial pattern of basal melting and together with local melt rate data resolve a disagreement between existing melt rate estimates from remote-sensing methods.

1. Introduction

Totten Glacier is a major outlet glacier of the East Antarctic Ice Sheet, draining approximately 3.9 m of sea-level equivalent (Morlighem et al., 2020). Remote sensing observations indicate that the region is presently undergoing thinning as well as grounding line retreat (X. Li et al., 2015; T. Li et al., 2023). Oceanographic observations have shown that warm modified circumpolar deep water is able to access the sub-ice shelf cavity and cause high melt rates (Rintoul et al., 2016). Additionally, recent numerical studies have suggested the potential for significant retreat of Totten Glacier over the next century (Pelle et al., 2021). Improved in-situ constraints, in particular the rate of ice-shelf basal melting and the shape of the sub-ice shelf cavity, are required to better understand both the ongoing and future evolution of this glacier system.

Bathymetry beneath ice shelves exerts control on their evolution in two primary ways. First, topographic highs result in regions where regrounding can occur, allowing for the formation of ice rises or rumples that can provide resistance to flow of upstream grounded ice. Second, the shape of the ocean cavity beneath ice shelves can significantly influence ocean circulation and regulate the spatial pattern of melting. Satellite-derived estimates indicate that Totten Ice Shelf (TIS) experiences rates of basal melting that are unusually high for East Antarctica (Depoorter et al., 2013; Rignot et al., 2013; Roberts et al., 2018b) and also strong inter-annual variability (Adusumilli et al., 2020). However, there are substantial disagreements in the spatial pattern of basal melting between the presently available products (Figures 1a–1c), and only a single in-situ observation of basal melting exists near the grounding zone of Totten Glacier (Vaňková, Cook, et al., 2021). Furthermore, the strong inter-annual variability inferred by Adusumilli et al. (2020) at Totten has not yet been validated, and elsewhere in Antarctica this dataset consistently overestimates the amplitude of inter-annual variability by up to an order of

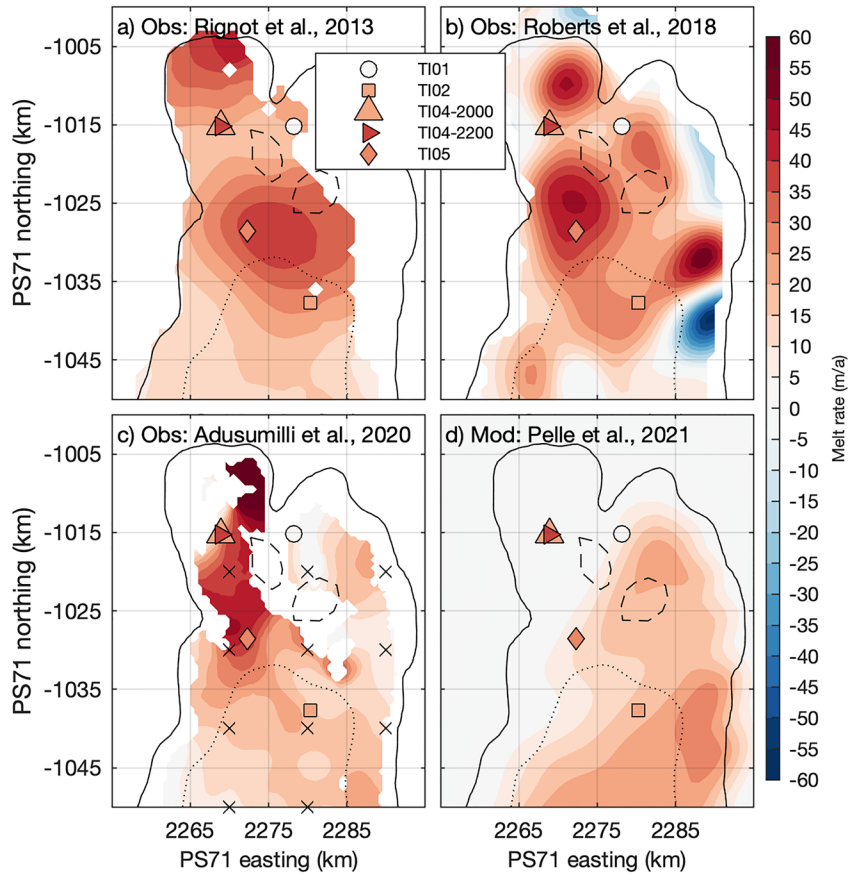

Figure 1. Satellite-derived and modeled melt rates for the back of the Totten Ice Shelf cavity. Satellite estimates from three available products; (a) Rignot et al. (2013), (b) Roberts et al. (2018b), and (c) Adusumilli et al. (2020). (d) Modeled melt rates from Pelle et al. (2021), year 2017 in their control run. ApRES-derived mean melt rates from the four observed sites over the 2017–2018 period are shown as color-filled symbols; for TI04 there are two estimates, one for 2,000 m and the other for 2,200-m ice thickness assumption. Grid cells for which Adusumilli et al. (2020) estimates quarter-yearly melt rate variability are marked by black crosses. In solid black is the grounding line from BedMachine (Morlighem et al., 2020), in dashed black the rumples from Roberts et al. (2018b), and in dotted black the hydrostatic line from ASAID (Bindschadler et al., 2011). The plots are on a polar stereographic (PS) projection grid.

magnitude (Vaňková & Nicholls, 2022). Finally, ice-sheet models are sensitive to regrounding on rumples near the Totten grounding line (McCormack et al., 2021; Pelle et al., 2020, 2021), with modeled melt rates in coupled ice-sheet ocean simulations resulting in a strong grid east-west melt rate gradient of opposite sign to that found in some of the satellite derived observations (Figures 1c and 1d).

Here we present new in-situ time series of ice-shelf basal melt and an updated bathymetry model for the region of Totten Glacier's grounding zone. The basal melt observations derived at four locations using 2-year long autonomous phase-sensitive radar (ApRES) observations confirm previous inferences of strong spatial and temporal variability. The bathymetry model is derived using an updated compilation of airborne gravity measurements and recently acquired active source seismic measurements of water-column thickness. The new bathymetry model shows that the strong spatial variability we observe in ice-shelf basal melt is associated with variations in water column thickness.

2. Data and Methods

2.1. Ice-Shelf Basal Melt From ApRES

Four ApRES were deployed on TIS to monitor basal melting at the back of the ice-shelf cavity. Sites TI01 and TI02 are located on the grid-eastern part of the ice shelf and sites TI04 and TI05 on its grid-western side

19448007, 2023, 10, Downloaded from https://agupubs.onlinelibrary.wiley.com/doi/10.1029/2023GL102960 by British Antarctic Survey, Wiley Online Library on [15/01/2025]. See the Terms and Conditions (https://onlinelibrary.wiley.com/terms-and-conditions) on Wiley Online Library for rules of use; OA articles are governed by the applicable Creative Commons License

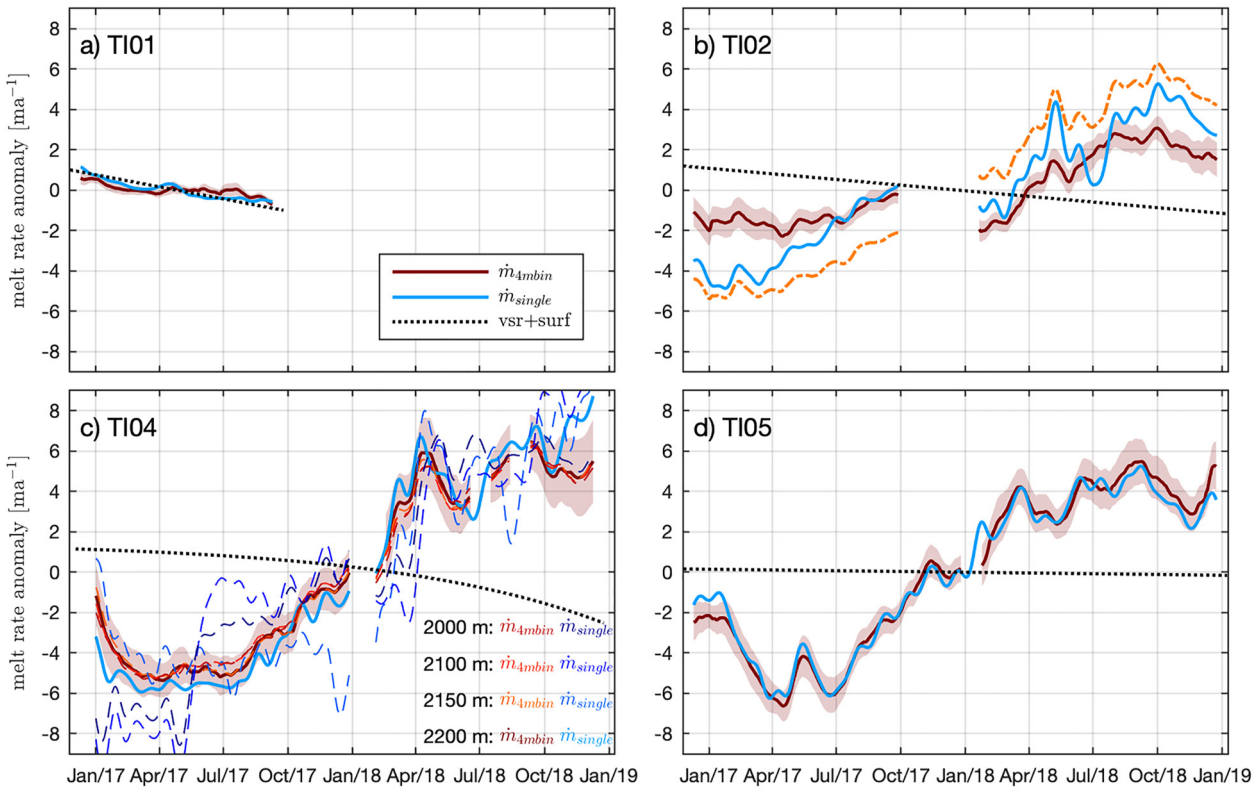

Figure 2. ApRES-derived basal melt rate anomaly. In blue (red) are the time series derived using the single-large-bin (4-m-bin-averaging) method, with shading showing uncertainty. The orange dash-dotted line at TI02 in (b) averages time series from the two methods and offsets segments around the data gap by 4.2 m/a to achieve a steady melt rate increase, as for TI04 and TI05. Multiple dashed lines in (c) indicate melt rate anomaly obtained assuming different ice thickness for TI04. Ice thicknesses are listed in black text with corresponding time series in red (blue) tones for the 4-m-bin-averaging (single-large-bin) method. In (c), solid lines show melting for the most likely TI04 ice thickness of 2,200 m. The black dotted line in all panels indicates the thickness anomaly from vertical strain and firn densification processes combined.

(Figure 1). The instruments were deployed in December 2016, serviced and redeployed in January 2018, and cleared in January 2019. When the ApRES were serviced in January 2018, a new pair of antennas was deployed and oriented along a line that was rotated 45° to the original setup. All instruments sampled at 90-min intervals. Instrument TI01 has data for only the first 9 months, TI02 has a data gap between October 2017 and January 2018, TI04 has a month-long data gap at the beginning of 2018, and TI05 has two full years of data (Figure 2).

ApRES measures positions of reflectors within the ice column and at its base, allowing estimation of basal melt rate (Nicholls et al., 2015). Temporal changes in the reflector positions can be detected with millimeter precision, enabled by accurate measurements of the phase of the reflected signal (Brennan et al., 2014). At each time step the ApRES return signal provides a range profile of amplitudes and phases. Each 4-m range interval of the complex signal is cross-correlated for each pair of consecutive time shots, yielding a stack of vertical displacement times series (Stewart, 2018; Vaňková et al., 2020). Reflector displacements over time are measured in a Lagrangian frame of reference; therefore, to derive a basal melt rate, first the thickness changes induced by internal ice dynamics and near surface processes were removed from total thickness changes following Jenkins et al. (2006) and Nicholls et al. (2015).

Because the TIS base is complex and often features multiple reflections (Vaňková, Cook, et al., 2021), we use two slightly different methods to derive the final melt rates (see Text S1 in Supporting Information S1 for details). Both methods utilize not only the first basal reflection, but also off-nadir reflections from the ice base that are located at more distant ranges. The first method (4-m-bin-averaging, $\dot{m}_{4mbin}$), following Vaňková, Cook, et al. (2021), derives a melt rate estimate for each time series, formed by cross-correlating 4-m range intervals that lie on the basal reflector. The final melt rate estimate is obtained by averaging the equally weighted individual estimates. The second method (single-large-bin, $\dot{m}_{single}$), for example, following Vaňková, Nicholls,

19448007, 2023, 10, Downloaded from https://agupubs.onlinelibrary.wiley.com/doi/10.1029/2023GL102960 by British Antarctic Survey, Wiley Online Library on [15/01/2025]. See the Terms and Conditions (https://onlinelibrary.wiley.com/terms-and-conditions) on Wiley Online Library for rules of use; OA articles are governed by the applicable Creative Commons License

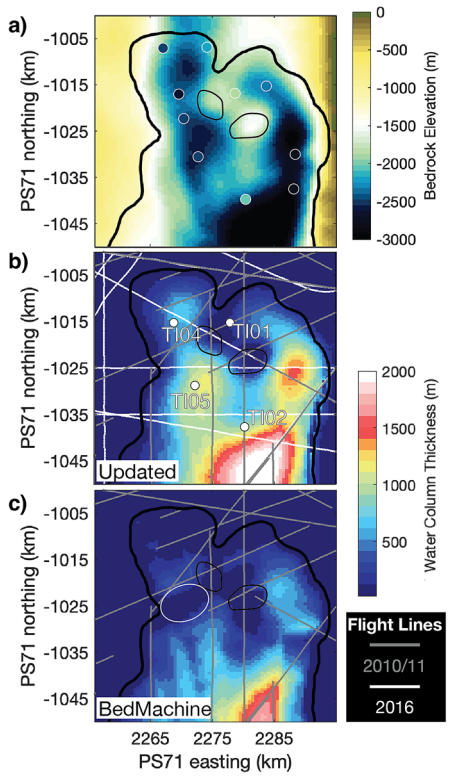

Figure 3. Updated bathymetry near the Totten grounding zone. (a) Modeled bedrock elevation. The thick black line denotes the BedMachine v3 grounding line. The thin black lines outline the location of two ice rumples (Roberts et al., 2018b) determined by examining height above flotation. All elevations inland of the grounding line are taken from BedMachine v3. Circles show bedrock elevation estimates from active source seismic measurements. (b) Updated gravity derived water-column thickness. White circles show the locations of the ApRES measurements. (c)Water-column thickness from BedMachine Antarctica v3 product. The white ellipse outlines a region of minimal water-column thickness which both promotes ice-sheet grounding and a barrier to ocean circulation in ice-ocean models (Pelle et al., 2021). In both b and c gray and white lines show geophysical flights containing gravity observations that were used to constrain the each bathymetry inversion. Note the additional lines available for our current study.

et al. (2021), derives a single melt rate estimate for a time series produced by cross-correlating through time a much larger depth range that contains all off-nadir basal reflectors. When all the 4-m-bin basal reflections show the same changes in range, then both methods yield identical results. When a dominant basal reflector behaves differently to the majority of the time series, the two estimates will differ, because the single-large-bin method implicitly gives larger weights to stronger reflectors, while the 4-m-bin-averaging weights all reflectors equally. Where the method for estimating melt rate is unspecified, the reported values refer to an average of the two methods ($\dot{m}$). The final melt rate time series were smoothed using a 30-day low pass filter; any shorter term variations in melting, including at tidal timescales, were lower in amplitude than the uncertainty on the variability.

2.2. Bathymetry Inversion From Gravity Observations and Seismic Constraints

We utilize both gravity and seismic observations to refine our understanding of bathymetry near the Totten Glacier grounding zone. We use geolocated gravity anomalies collected by the Investigating the Cryospheric Evolution of the Central Antarctic Plate project during 2009/1010, 2010/2011, and 2016/2017 field seasons. These data were collected via a BT-67 fixed-wing aircraft and were smoothed with a 150-s filter to suppress noise, resulting in minimum resolved spatial wavelengths of 6.25 km. Observations from 2009/2010 and 2010/2011 (Figure 3c) were used in an earlier study that derived bathymetry beneath TIS (Greenbaum et al., 2015). The 2016/2017 survey provides additional coverage near the grounding zone (Figure 3b), thus motivating our new analysis.

We collected 11 active source seismic observations (see Figure 3a and Figure S8a in Supporting Information S1 for locations) of water column thickness during January of 2019 to complement the aerogeophysical datasets. A small explosive charge (~500g), buried in a shallow hole (<1 m), was used as the source and recorded using a 240-m long 24-channel geophone string. We estimated the water column thickness by measuring both the ice-bottom reflection and sea-bed reflection. Errors in water column thickness that arise from uncertainty in seawater seismic velocities and tidal variations will be less than 10 m (Brisbourne et al., 2020) and small compared with uncertainties from gravity derived inversions discussed below.

A source of uncertainty common to all gravity-derived bathymetric models is bedrock density. Ideally, seismic observations would be used to provide tie points during the inversion. However, our relatively sparse seismic observations are not well suited to this purpose since both the gravity observations and seismic observations spatially alias short (<10 km) wavelength topographic features. Thus, we model the bathmetry via a two step-process. First, we use the gravity observations to invert for bathymetry using a range of bedrock densities. Second, we calculate the mistfit between each gravity derived bathymetry model at the locations were we collected seismic observations to choose the optimal model.

We model the gravity signal as the sum of three layers: ice ($\rho = 920$ kg/m^3), ocean ($\rho = 1{,}030$ kg/m^3), and bedrock. We approximate the model domain as a series of 2-km rectangular prisms and calculate the gravitational effect of each prism using the method of Blakely (1995) (subroutine B.6) with the ice geometry taken from BedMachine v3 (Morlighem et al., 2020). Prior to the inversion, we remove the influence of long-wavelength signals (such as those from the Moho and deep sedimentary basins). Similar to previous studies (An et al., 2019), we first calculate the misfit between a forward model constructed using the BedMachine ice thickness data and the observed gravity field at grounded locations. A smoothed version of the misfit function is then subtracted from all observations (including those over the floating ice shelf) for use in the inversion (Figure S7 in Supporting Information S1). We use the resulting gravity observations to estimate bathymetry by performing a constrained (i.e., the top of the ice

19448007, 2023, 10, Downloaded from https://agupubs.onlinelibrary.wiley.com/doi/10.1029/2023GL102960 by British Antarctic Survey, Wiley Online Library on [15/01/2025]. See the Terms and Conditions (https://onlinelibrary.wiley.com/terms-and-conditions) on Wiley Online Library for rules of use; OA articles are governed by the applicable Creative Commons License

Table 1
Time-Mean Melt Rate for a Given Ice Thickness H at Each Site

	H (m)	$\dot{m}$ (m/a)	$\dot{m}_{4mbin}$ (m/a)	$\dot{m}_{single}$ (m/a)
TI01	1,936	0.4 ± 0.6	0.5 ± 0.5	0.3 ± 0.4
TI02	1,470	21.3 ± 3.5	22.2 ± 2.2	20.4 ± 2.1
TI04	2,000	21.7 ± 10.5	27.0 ± 5.5	16.4 ± 4.5
TI04	2,100	24.6 ± 11.2	30.6 ± 5.2	18.6 ± 4.8
TI04	2,150	30.4 ± 8.2	33.1 ± 5.3	27.6 ± 5.0
TI04	2,200	35.9 ± 6.3	34.8 ± 5.5	37.0 ± 5.2
TI05	1,910	25.1 ± 4.2	25.4 ± 3.7	24.8 ± 3.5

Note. Results from both methods, 4-m-bin-averaging ($\dot{m}_{4mbin}$) and single-large-bin ($\dot{m}_{single}$), and their average ($\dot{m}$) are included. Given the uncertainty about the ice-base location at TI04, melt rates for multiple possible ice thicknesses are listed, the most likely thickness being 2,200 m.

layer cannot be above the ice bottom) least-squares inversion using 2nd-order Tikhonov regularization (for example, Chapter 4 of Aster et al., 2018) with the smoothness parameter chosen from a cross-validation curve (Figure S6 in Supporting Information S1). We use the BedMachine grounding line as well the location the of two ice rumples (Roberts et al., 2018b), that is, areas where surface elevation are above their height-above-flotation, to define regions of floating ice where a water layer is allowed in the inversion. Due to the variety of survey altitudes and variable spatial resolution of the data, we chose to calculate the gravity effect at the geolocation and flight altitude of each observation to avoid introducing artifacts during gridding.

3. Results

3.1. Basal Melt Rate

The ApRES mean melt rate estimates range from 0.4 m/a at TI01 to over 20 m/a at the remaining three sites (Table 1). For all sites, the uncertainties in the mean melt rates are much larger than typically found in previous ApRES surveys (usually less than 0.1 m/a). This is primarily due to large uncertainties in the vertical strain rate profile; a consequence of poor internal reflections in the bottom half to a third of the ice column (Figure S1 in Supporting Information S1). TI01 has the lowest uncertainty (0.6 m/a), because its ice base is relatively flat and vertical strain rate constant with depth, while at the remaining sites, the strain rate varies with depth. TI04 has the largest uncertainties (∼10 m/a), caused by the heterogeneity of the ice base, where the tracking of different basal reflectors suggests different rates of melting (Figure S5 in Supporting Information S1) and estimates from the two methods ($\dot{m}_{4mbin}$ and $\dot{m}_{single}$) differ substantially (Table 1). The final complexity for TI04 is the presence of steeply sloped off nadir reflectors. As a result there are multiple possibilities for the reference ice thickness, between 2,000 and 2,200 m. Altogether, the corresponding mean melt rate estimates at TI04 range from 22 to 36 m/a, depending on the assumed ice thickness, with some indirect evidence from tidal motion suggesting that the higher-end melt rate estimate is more likely (Text S1.3 in Supporting Information S1). In either case, the mean melt rate estimate at TI04 is comparable to TI05 and TI02, and at least 20 m/a higher than at TI01.

Melt rate variability estimates for the four sites are shown in Figure 2 as anomalies centered around 0 m/a. This is to highlight that although the uncertainties in the mean melt rates are high, uncertainties in the melt rate variability are much lower (at most ∼1 m/a). The non-melt rate contributions to the total change in thickness from vertical strain rate and near-surface processes can amount to up to 3.5 m over the course of two years (dotted lines in Figure 2) as in the case of TI04, but this value is small compared with the year-to-year variability in basal melting.

The two different methods for estimating melt rate variability agree well at sites TI01, TI05, and also at TI04 for the assumption of 2,200 m ice thickness. An agreement between the methods means that the basal reflectors experience the same changes, and thus the estimates of melt rate variability at these sites are representative for the basal area within the ApRES view (circle with radius of ∼1 km). At TI04 the two methods show differences in shorter term variability for ice thickness assumptions of 2,000, 2,100 and 2,150 m, which means that some strong reflectors near those ranges undergo variations that are different from the bulk variation. Interestingly, $\dot{m}_{4mbin}$ is the same for all plausible ice thicknesses at TI04. Therefore, while the ice-thickness assumption causes large uncertainty in the mean melt rate estimates at TI04, it has little effect on the uncertainty on temporal melt rate variability (Figure 2c). At TI02 the first basal reflector shows much higher amplitude of variability than the more distant reflectors (Figure S4a in Supporting Information S1). As a result, at this site the $\dot{m}_{single}$ time series, being dominated by the first strong reflector, has a larger variability than the $\dot{m}_{4mbin}$ time series (Figure 2b).

Melt rates at TI01 show relatively little variability, with a nearly linear melt rate decrease of less than 2 m/a over the 9-month record (Figure 2a). At the three remaining sites melt rates vary greatly between the two observed years (Figures 2b–2d). The melt rate variability at TI04 and TI05 is almost identical (Figures 2c and 2d); first a melt rate decrease between January and April 2017 by ∼4 m/a, then a steady melt rate increase between July 2017 and September 2018 by ∼12 m/a, and finally melt rates plateauing or slightly increasing until January 2019. The variability at TI02 is similar, except the melt rate increase begins earlier (Figure 2b). The TI02 melt rate time series further suggest a melt rate decrease some time during a data gap between October 2017 and January 2018,

19448007, 2023, 10, Downloaded from https://agupubs.onlinelibrary.wiley.com/doi/10.1029/2023GL102960 by British Antarctic Survey, Wiley Online Library on [15/01/2025]. See the Terms and Conditions (https://onlinelibrary.wiley.com/terms-and-conditions) on Wiley Online Library for rules of use; OA articles are governed by the applicable Creative Commons License

however, this is most likely an artifact caused by a change in antenna orientation during a revisit in January 2018 on what is a very complicated and heterogeneous basal reflector. Both end points of the October 2017/January 2018 gap in data indicate a continued steady melt rate increase over this time period, as would be the case if TI02 experienced the same inter-annual melt rate variability pattern as TI04 and TI05. A TI02 melt rate time series obtained by averaging results from the two different methods and offsetting time series from each year to achieve a steady melt rate increase over the data gap is shown by orange dash-dotted line in Figure 2b. This melt rate time series now resembles those from TI04 and TI05 in both the variability and its amplitude. There is also higher-frequency variability that is consistent across the three sites, in particular during 2018; there is local melt rate maximum between April and May 2018 followed by a pronounced local melt rate drop by 1–3 m/a until July 2018. Since all three sites show similar timing and amplitude of melt rate variability at monthly timescales, it is likely that their inter-annual variability is also comparable, in which case, the offset orange dash-dotted line in Figure 2b would provide a more realistic estimate of melt rate variability for TI02 than either of the two raw time series.

3.2. Updated Bathymetry

Our preferred bathymetric model results from an inversion using a bedrock density of ($\rho = 2{,}500$ kg/m^3) (Figures 3a and 3b and Figure S8b in Supporting Information S1). Again, the seismic observations were not used to constrain the inversion but are used to select the preferred model by calculating the mean absolute misfit between the gravity and seismic bedrock elevation inversions across a range of densities. We observe a well-defined minimum for a bedrock density of ($\rho = 2{,}500$ kg/m^3) where the mean absolute error is 6 m with standard deviation of the misfit of ~270 m, comparable to previous studies (for example, Studinger et al., 2004). The dominant source of these discrepancies is likely the result of the long-wavelength nature of the bathymetry model that arises from both the frequency content of the gravity observations and the smoothing induced by the regularization during the inversion process. Additionally, misfit will be impacted by variations in bedrock density that were not accounted for by gravity shift adjustments as well as errors in gravity field (~6 mgals), which introduces a ~100 m uncertainty for a density contrast of 1,500 kg/m^3. Thus, given these inherent limitations of the method, relatively large (up to 400 m) deviations from this model are to be expected.

Similar to the model of Greenbaum et al. (2015) (which formed a basis of the BedMachine dataset at Totten), near the grounding line our bathymetric model has a grid north-south ridge that extends approximately 20 km downstream of the grounding line (Figures 3a and 3c.), generating several ice rumples that influence ice flow (Roberts et al., 2018b). Our model differs from that of Greenbaum et al. (2015) in two significant ways. First, the mean depth in our model is significantly greater (~380 m deeper on average), which is in part due to the lower bedrock density used in our preferred inversion ($\rho = 2{,}500$ kg/m^3 vs. $\rho = 2{,}700$ kg/m^3). A commensurate higher mean absolute misfit (~400m) between our seismic bedrock estimates and those of Greenbaum et al. (2015) is also observed. Second, the incorporation of the additional airborne gravity measurements used in our study have improved the resolution. For example, a prominent bathymetric high located to the grid west of the rumples in the Greenbaum et al. (2015) model is absent in our bathymetric model (white ellipse in Figure 3c).

4. Discussion

4.1. Spatial Melt Rate Pattern

The ApRES measurements show that there are large spatial differences in mean melt rates across the back of the TIS cavity. Despite the high uncertainty, melt rates at TI04 of ~22–36 m/a contrast with very low melting at TI01 of only ~0.4 m/a. The same grid east-west gradient in melting at the back of the cavity is also captured in the most recent satellite-derived mean melt rates of Adusumilli et al. (2020) (hereafter, A2020), but it is missing in the two older products of Rignot et al. (2013) and Roberts et al. (2018b) (Figure 1).

The rate of basal melting is typically understood to be proportional to the product of water flow speed and thermal driving, the difference between in-situ temperature and in-situ freezing point (for example, Jenkins et al., 2010), with additional complexities potentially arising in quiescent environments with strong stratification (Davis et al., 2023). Therefore, the very low melt rates at TI01, and along the grid-eastern grounding line in A2020, mean that the ocean temperature or the flow speed must be much lower there compared with the remaining sites.

The grid east-west gradient in the melt rates near the TIS grounding line from A2020, supported by our in-situ melt rate estimates, can be understood physically using our updated bathymetry. On the grid-eastern side, where

19448007, 2023, 10, Downloaded from https://agupubs.onlinelibrary.wiley.com/doi/10.1029/2023GL102960 by British Antarctic Survey, Wiley Online Library on [15/01/2025]. See the Terms and Conditions (https://onlinelibrary.wiley.com/terms-and-conditions) on Wiley Online Library for rules of use; OA articles are governed by the applicable Creative Commons License

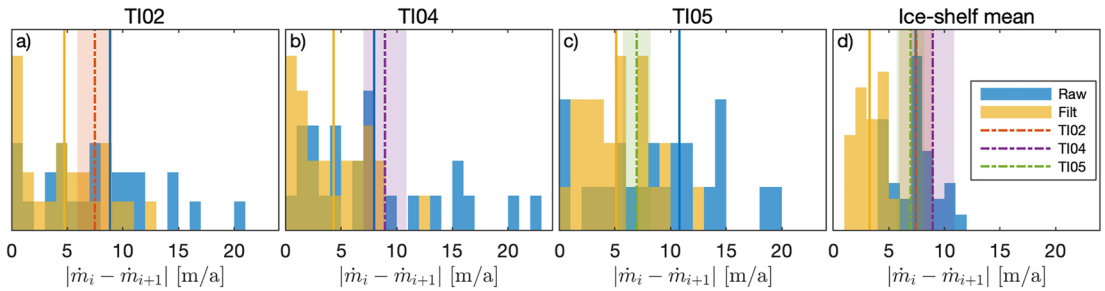

Figure 4. Year-to-year melt rate difference in ApRES and satellite data. (a–c) Histogram shows year-to-year melt rate difference for all available years in Adusumilli et al. (2020) at the grid point nearest to each ApRES site; blue (yellow) uses quarterly (3-year low-pass filtered) time series and respective solid lines show means of each distribution. Dash-dotted line shows melt rate difference between years 2017 and 2018 observed using ApRES. (d) Mean year-to-year melt rate difference at each available point across the back of Totten Ice Shelf (crosses in Figure 1c).

the melt rates are low (TI01, Figure 1c), the bedrock is relatively shallow (Figure 3a) and the water column only ∼100 m thick (Figure 3b). On the grid-western side, where the melt rates are high (TI04), the bedrock is several hundred meters deeper and the water column several hundred meters thick. This previously unknown trough (Figure 3c) connecting TI04 to the rest of the cavity, is able to conduct warm water located at depth toward the grid-western grounding line. Bathymetry also acts to block warm water access to TI01 and the grid-eastern grounding line. Furthermore, the grid-eastward reduced water column thickness (Figure 3b) acts together with the rumples and partially grounded area between TI01 and TI04 to shield the grid-eastern portion of the TIS grounding line from the clockwise cavity circulation (for example, Gwyther et al., 2014). Thus the combination of reduced flow speeds due to circulation cutoff and lower temperatures due to bathymetric obstacles lead to low melt rates at TI01 and the TIS grid-eastern grounding line in general.

4.2. Temporal Melt Rate Variability

Focusing on sites TI02, TI04, and TI05, that have melt rate records from both years, we observe weaker melting in 2017 and stronger melting in 2018 at all three locations, with a year-to-year variability (difference between mean annual melt rate in consecutive years) of 7–9 m/a (Figures 2b–2d). Although observations of melt rate evolution are still relatively sparse, this is the highest inter-annual melt rate variability observed anywhere in Antarctica to date. The 2-year long time series show no sign of a seasonal cycle and indicate that either the dominant time scale of variability at the back of the TIS cavity is inter-annual, or we have sampled a time period with anomalous forcing from the continental shelf. Because we have not identified any evidence of the latter, we focus on investigating the inter-annual timescales of melt rate variability. The importance of these is supported by previous observational and modeling studies (Greene et al., 2017; Gwyther et al., 2018; Nakayama et al., 2021).

For longer-term context, we examine the A2020 satellite-derived melt rate time series. However, as these data have not been validated for TIS, we need to carry out a comparison with any available data. This is especially important, because for the only published location with time series comparison between A2020 and ApRES, the low melting Filchner-Ronne Ice Shelf, A2020 was found to overestimate inter-annual variability by up to an order magnitude with no correspondence between the timing of the satellite-derived variability and that from in-situ measurements (Vaňková & Nicholls, 2022). First, we find that melt rates co-vary in phase both for the three ApRES sites, and at the back of the TIS cavity in A2020 (Figure S12a in Supporting Information S1). In-phase variability across the back of TIS is consistent with the spatial pattern of the dominant mode of variability according to the model of Gwyther et al. (2018). Second, we find that the A2020 melt rate time series at TIS correlate strongly with the curl of the wind stress at the continental shelf (Figure S12a in Supporting Information S1), consistent with the mechanism of Greene et al. (2017). The mechanism implicates (unobserved) warm water inflow and associated melt rate increase as the connecting pieces that communicate (observed) inter-annual changes in wind forcing above the continental shelf to (observed) corresponding changes in ice flow speed.

Having found that the characteristic timescales and the phasing of variability in A2020 are consistent with other data and models, we assume that the amplitude of year-to-year variability in A2020 is also accurate and use these time series to place the ApRES-observed variability in a longer-term context. We construct histograms of year-to-year melt rate difference for each TIS site for both datasets (Figures 4a–4c). For A2020 this results in 25 points, since there are 26 years of data available, while for ApRES there is only a single point given by the difference of the two

19448007, 2023, 10, Downloaded from https://agupubs.onlinelibrary.wiley.com/doi/10.1029/2023GL102960 by British Antarctic Survey, Wiley Online Library on [15/01/2025]. See the Terms and Conditions (https://onlinelibrary.wiley.com/terms-and-conditions) on Wiley Online Library for rules of use; OA articles are governed by the applicable Creative Commons License

available years. The A2020 time series are available every 10 km (Figure 1c), and we use the time series from the grid point nearest to each ApRES site. The ApRES-observed mean annual melt rate difference between years 2017 and 2018 falls well within the range of satellite-observed year-to-year variations over the course of the 26 observed years. The in-situ observations lie near the mean of the distributions for the unfiltered A2020 time series and are higher, but still within the observed range, than average for their 3-year low-pass filtered version (Figure 4d). This implies that if the amplitude of year-to-year variability in A2020 is accurate, the 7–9 m/a ApRES-observed melt rate difference between 2017 and 2018 is typical for TIS. Therefore we have most likely observed in-situ only a part of a longer period cycle and cannot attribute the large year-to-year melt rate change to an anomalous forcing.

While the ApRES-observed melt rates can be obtained from the parameterization of Jenkins et al. (2010) for a number of realistic combinations of temperatures and flow speeds, as observed in front of TIS by Rintoul et al. (2016), the problem of inferring required temperature and flow speed changes necessary to produce the observed melt rate change is relatively under-constrained (Text S2 in Supporting Information S1). In absence of strong stratification, the melt rate increase is proportional to the increase of the product between flow speed and thermal driving, however, the proportionality constant is strongly dependent on the drag coefficient (C_D) that controls the rate of heat transfer from the ocean to the ice base. C_D can vary widely and few measurements exist. Assuming a C_D value measured at the Ronne Ice Shelf (Jenkins et al., 2010), the melt rate increase of 8 m/a could be explained either by 0.4–0.6°C temperature increase, or by 1–3 cm/s flow speed increase (Figure S11 in Supporting Information S1). For a rougher base, associated with higher C_D, which may be more realistic in close proximity to the TIS grounding line, the increase in flow speed and temperature needs to be smaller to achieve the same melt rate change.

Finally, we note that in the A2020 dataset the TIS melt rate time series exhibit by far the highest variance from all of Antarctica (Figure S12b in Supporting Information S1). Thus our indirect validation of the inter-annual variability in the A2020 time series from TIS is not necessarily transferable to other ice shelves. It also does not transfer to other timescales. For example, while the ApRES data do not show significant seasonal variability, A2020 has a strong seasonal signal. As a result, the detectability threshold of temporal melt rate variability using satellite methods still remains to be determined.

4.3. Implications of Updated Bathymetry

The most significant feature of our updated bathymetric model is the lack of a broad bathymetric ridge to the grid west of the of the ice rumples that produces a relatively thin water column (<50 m) in the BedMachine product. While some uncertainties remain, the presence of this broad bathymetric high is incompatible with the updated set of gravity and seismic observations. In simulations of Totten Glacier's future evolution, this bathymetric ridge influences model behavior in two significant ways. First, this relatively shallow bathymetry results in grounding of the ice shelf that applies back stress to upstream grounded ice and reduces the rate of retreat (Pelle et al., 2020, 2021). Second, as discussed above in Section 4.1, this ridge acts as a barrier to warm water intrusions and as a result can modulate the rate of grounding line retreat (Pelle et al., 2021). Thus, simulations with our updated bathymetric model will likely modify our understanding of the region's future evolution.

5. Conclusions

In-situ melt rate measurements at TIS proved to be key for validating remotely-derived melt rate products. Updated bathymetry, constrained by local seismic measurements, uncovered a previously unknown trough and provided a physical explanation for a grid east-west melt rate gradient near the TIS grounding zone that was inferred by the ApRES data and one of the three available satellite-derived products (Adusumilli et al., 2020). The updated bathymetry may solve previous problems with regrounding in ice sheet simulations due to erroneously shallow bedrock in the TIS region and therefore result in more accurate sea-level projections (Pelle et al., 2021). Both the bathymetry and melt rates will lead to better constrained models of Totten sub-ice shelf circulation and melting. The dominant time scales of variability at TIS are inter-annual; in-situ melt rate monitoring at this and similar ice shelves will therefore require sustained multi-year monitoring.

Data Availability Statement

All gravity data used in this study are available at National Snow and Ice Data Center (Blankenship et al., 2011, updated 2014) and the Australian Antarctic Data Center (Roberts et al., 2018a). All seismic data are available at the IRIS-Data Management Center (https://ds.iris.edu/mda/20-017/). The raw ApRES data are available at

19448007, 2023, 10, Downloaded from https://agupubs.onlinelibrary.wiley.com/doi/10.1029/2023GL102960 by British Antarctic Survey, Wiley Online Library on [15/01/2025]. See the Terms and Conditions (https://onlinelibrary.wiley.com/terms-and-conditions) on Wiley Online Library for rules of use; OA articles are governed by the applicable Creative Commons License

Australian Antarctic Data Center (Galton-Fenzi & Cook, 2023). The melt rate time series, updated bathymetry, as well as code used for the gravity inversion and ApRES processing are available at https://doi.org/10.6084/m9.figshare.21824580. The ApRES processing scripts are also available at the following repository, https://github.com/irenavankova/ApRES_processing.

Acknowledgments
This project received grant funding from the Australian Government as part of the Antarctic Science Collaboration Initiative program and the Australian Research Council's Special Research Initiative for Antarctic Gateway Partnership (Project ID SR140300001). Field activities were supported through the Australian Antarctic Science Program Grant 4436. I.V. received funding for this work from the European Union's Horizon 2020 research and innovation programme under the Marie Skłodowska-Curie Grant agreement No. 790062 and from the Laboratory Directed Research and Development program of Los Alamos National Laboratory under project number 20220812PRD4. J.P.W. received partial support from National Science Foundation Grant OPP-1914767. Some of the seismic instrumentation was provided by the Incorporated Research Institutions for Seismology (IRIS) through the PASSCAL Polar Support Services. We thank Reinhard Drews and an anonymous reviewer for their input that improved the paper.

References

Adusumilli, S., Fricker, H. A., Medley, B., Padman, L., & Siegfried, M. R. (2020). Interannual variations in meltwater input to the Southern Ocean from Antarctic ice shelves. *Nature Geoscience*, *13*(9), 1–5. https://doi.org/10.1038/s41561-020-0616-z

An, L., Rignot, E., Chauche, N., Holland, D. M., Holland, D., Jakobsson, M., et al. (2019). Bathymetry of Southeast Greenland from Oceans Melting Greenland (OMG) data. *Geophysical Research Letters*, *46*(20), 11197–11205. https://doi.org/10.1029/2019GL083953

Aster, R. C., Borchers, B., & Thurber, C. H. (2018). *Parameter estimation and inverse problems*. Elsevier.

Bindschadler, R., Choi, H., & Collaborators, A. (2011). *High-resolution image-derived grounding and hydrostatic lines for the Antarctic ice sheet*. U.S. Antarctic Program (USAP) Data Center. https://doi.org/10.7265/N56T0JK2

Blakely, R. J. (1995). *Potential theory in gravity & magnetic applications*. Cambridge University Press. https://doi.org/10.1017/S0016756800008773

Blankenship, D. D., Young, D. A., Richter, T. G., & Greenbaum, J. S. (2011). *Icebridge BGM-3 gravimeter L2 geolocated free air anomalies, version 1*. NASA National Snow and Ice Data Center Distributed Active Archive Center. Updated 2014. https://doi.org/10.5067/8DJW56PKY133

Brennan, P. V., Lok, L. B., Nicholls, K., & Corr, H. (2014). Phase-sensitive FMCW radar system for high-precision Antarctic ice shelf profile monitoring. *Sonar Navigation IET Radar*, *8*(7), 776–786. https://doi.org/10.1049/iet-rsn.2013.0053

Brisbourne, A., Kulessa, B., Hudson, T., Harrison, L., Holland, P., Luckman, A., et al. (2020). An updated seabed bathymetry beneath Larsen C Ice Shelf, Antarctic Peninsula. *Earth System Science Data*, *12*(2), 887–896. https://doi.org/10.5194/essd-12-887-2020

Davis, P. E. D., Nicholls, K. W., Holland, D. M., Schmidt, B. E., Washam, P., Riverman, K. L., et al. (2023). Suppressed basal melting in the eastern Thwaites Glacier grounding zone. *Nature*, *614*(7948), 479–485. https://doi.org/10.1038/s41586-022-05586-0

Depoorter, M. A., Bamber, J. L., Griggs, J. A., Lenaerts, J. T. M., Ligtenberg, S. R. M., van den Broeke, M. R., & Moholdt, G. (2013). Calving fluxes and basal melt rates of Antarctic ice shelves. *Nature*, *502*(7469), 89–92. https://doi.org/10.1038/nature12567

Galton-Fenzi, B. K., & Cook, S. (2023). Autonomous phase sensitive radar (ApRES) on Totten Glacier 2016-2019 (Version 2) [Dataset]. Australian Antarctic Data Centre. https://doi.org/10.26179/BGNV-4H81

Greenbaum, J. S., Blankenship, D. D., Young, D. A., Richter, T. G., Roberts, J. L., Aitken, A. R. A., et al. (2015). Ocean access to a cavity beneath Totten Glacier in East Antarctica. *Nature Geoscience*, *8*(4), 294–298. https://doi.org/10.1038/ngeo2388

Greene, C. A., Blankenship, D. D., Gwyther, D. E., Silvano, A., & van Wijk, E. (2017). Wind causes Totten Ice Shelf melt and acceleration. *Science Advances*, *3*(11), e1701681. https://doi.org/10.1126/sciadv.1701681

Gwyther, D. E., Galton-Fenzi, B. K., Hunter, J. R., & Roberts, J. L. (2014). Simulated melt rates for the Totten and Dalton ice shelves. *Ocean Science*, *10*(3), 267–279. https://doi.org/10.5194/os-10-267-2014

Gwyther, D. E., O'Kane, T. J., Galton-Fenzi, B. K., Monselesan, D. P., & Greenbaum, J. S. (2018). Intrinsic processes drive variability in basal melting of the Totten Glacier Ice Shelf. *Nature Communications*, *9*(1), 1–8. https://doi.org/10.1038/s41467-018-05618-2

Jenkins, A., Corr, H. F. J., Nicholls, K. W., Stewart, C. L., & Doake, C. S. M. (2006). Interactions between ice and ocean observed with phase-sensitive radar near an Antarctic ice-shelf grounding line. *Journal of Glaciology*, *52*(178), 325–346. https://doi.org/10.3189/172756506781828502

Jenkins, A., Nicholls, K. W., & Corr, H. F. J. (2010). Observation and parameterization of ablation at the base of Ronne Ice Shelf, Antarctica. *Journal of Physical Oceanography*, *40*(10), 2298–2312. https://doi.org/10.1175/2010JPO4317.1

Li, T., Dawson, G. J., Chuter, S. J., & Bamber, J. L. (2023). Grounding line retreat and tide-modulated ocean channels at Moscow University and Totten Glacier ice shelves, East Antarctica. *The Cryosphere*, *17*(2), 1003–1022. https://doi.org/10.5194/tc-17-1003-2023

Li, X., Rignot, E., Morlighem, M., Mouginot, J., & Scheuchl, B. (2015). Grounding line retreat of Totten Glacier, East Antarctica, 1996 to 2013. *Geophysical Research Letters*, *42*(19), 8049–8056. https://doi.org/10.1002/2015GL065701

McCormack, F. S., Roberts, J. L., Gwyther, D. E., Morlighem, M., Pelle, T., & Galton-Fenzi, B. K. (2021). The impact of variable ocean temperatures on Totten Glacier stability and discharge. *Geophysical Research Letters*, *48*(10), e2020GL091790. https://doi.org/10.1029/2020GL091790

Morlighem, M., Rignot, E., Binder, T., Blankenship, D., Drews, R., Eagles, G., et al. (2020). Deep glacial troughs and stabilizing ridges unveiled beneath the margins of the Antarctic ice sheet. *Nature Geoscience*, *13*(2), 132–137. https://doi.org/10.1038/s41561-019-0510-8

Nakayama, Y., Greene, C. A., Paolo, F. S., Mensah, V., Zhang, H., Kashiwase, H., et al. (2021). Antarctic slope current modulates ocean heat intrusions towards Totten Glacier. *Geophysical Research Letters*, *48*(17), e2021GL094149. https://doi.org/10.1029/2021GL094149

Nicholls, K. W., Corr, H. F., Stewart, C. L., Lok, L. B., Brennan, P. V., & Vaughan, D. G. (2015). A ground-based radar for measuring vertical strain rates and time-varying basal melt rates in ice sheets and shelves. *Journal of Glaciology*, *61*(230), 1079–1087. https://doi.org/10.3189/2015JoG15J073

Pelle, T., Morlighem, M., & McCormack, F. S. (2020). Aurora Basin, the weak underbelly of East Antarctica. *Geophysical Research Letters*, *47*(9), e2019GL086821. https://doi.org/10.1029/2019GL086821

Pelle, T., Morlighem, M., Nakayama, Y., & Seroussi, H. (2021). Widespread grounding line retreat of Totten Glacier, East Antarctica, over the 21st century. *Geophysical Research Letters*, *48*(17), e2021GL093213. https://doi.org/10.1029/2021GL093213

Rignot, E., Jacobs, S., Mouginot, J., & Scheuchl, B. (2013). Ice-shelf melting around Antarctica. *Science*, *341*(6143), 266–270. https://doi.org/10.1126/science.1235798

Rintoul, S. R., Silvano, A., Pena-Molino, B., van Wijk, E., Rosenberg, M., Greenbaum, J. S., & Blankenship, D. D. (2016). Ocean heat drives rapid basal melt of the Totten Ice Shelf. *Science Advances*, *2*(12), e1601610. https://doi.org/10.1126/sciadv.1601610

Roberts, J., Blankenship, D., Greenbaum, J., Beem, L., Kempf, S., Young, D., et al. (2018a). *EAGLE/ICECAP II - Geophysical observations (surface and bed elevation, ice thickness, gravity disturbance and magnetic anomalies), ver. 1*. Australian Antarctic Data Centre. https://doi.org/10.26179/5bcfffdabcf92

Roberts, J., Galton-Fenzi, B. K., Paolo, F. S., Donnelly, C., Gwyther, D. E., Padman, L., et al. (2018b). Ocean forced variability of Totten Glacier mass loss. *Geological Society, London, Special Publications*, *461*(1), 175–186. https://doi.org/10.1144/SP461.6

Stewart, C. L. (2018). Ice-ocean interactions beneath the North-Western Ross Ice Shelf, Antarctica (Thesis). University of Cambridge. https://doi.org/10.17863/CAM.21483

Studinger, M., Bell, R. E., & Tikku, A. A. (2004). Estimating the depth and shape of subglacial Lake Vostok's water cavity from aerogravity data. *Geophysical Research Letters*, *31*(12). https://doi.org/10.1029/2004GL019801

19448007, 2023, 10, Downloaded from https://agupubs.onlinelibrary.wiley.com/doi/10.1029/2023GL102960 by British Antarctic Survey, Wiley Online Library on [15/01/2025]. See the Terms and Conditions (https://onlinelibrary.wiley.com/terms-and-conditions) on Wiley Online Library for rules of use; OA articles are governed by the applicable Creative Commons License

Vaňková, I., Cook, S., Winberry, J. P., Nicholls, K. W., & Galton-Fenzi, B. K. (2021). Deriving melt rates at a complex ice shelf base using in situ radar: Application to Totten Ice Shelf. *Geophysical Research Letters*, *48*(7). https://doi.org/10.1029/2021GL092692

Vaňková, I., & Nicholls, K. W. (2022). Ocean variability beneath the Filchner-Ronne Ice Shelf inferred from basal melt rate time series. *Journal of Geophysical Research: Oceans*, *127*(10), e2022JC018879. https://doi.org/10.1029/2022JC018879

Vaňková, I., Nicholls, K. W., & Corr, H. F. J. (2021). The nature of ice intermittently accreted at the base of Ronne Ice Shelf, Antarctica, assessed using phase-sensitive radar. *Journal of Geophysical Research: Oceans*, *126*(10), e2021JC017290. https://doi.org/10.1029/2021JC017290

Vaňková, I., Nicholls, K. W., Corr, H. F. J., Makinson, K., & Brennan, P. V. (2020). Observations of tidal melt and vertical strain at the Filchner-Ronne Ice Shelf, Antarctica. *Journal of Geophysical Research: Earth Surface*, *125*(1). https://doi.org/10.1029/2019JF005280

References From the Supporting Information

Davis, P. E. D., & Nicholls, K. W. (2019). Turbulence observations beneath Larsen C ice shelf, Antarctica. *Journal of Geophysical Research: Oceans*, *124*(8), 5529–5550. https://doi.org/10.1029/2019JC015164

Haran, T., Bohlander, J., Scambos, T., Painter, T., & Fahnestock, M. (2021). *Modis mosaic of Antarctica 2003-2004 (MOA2004) image map, version 2*. NASA National Snow and Ice Data Center Distributed Active Archive Center.

Humbert, A., Christmann, J., Corr, H. F. J., Helm, V., Höyns, L.-S., Hofstede, C., et al. (2022). On the evolution of an ice shelf melt channel at the base of Filchner Ice Shelf, from observations and viscoelastic modeling. *The Cryosphere*, *16*(10), 4107–4139. https://doi.org/10.5194/tc-16-4107-2022

Middleton, L., Vreugdenhil, C. A., Holland, P. R., & Taylor, J. R. (2021). Numerical Simulations of melt-driven double-diffusive fluxes in a turbulent boundary layer beneath an ice shelf. *Journal of Physical Oceanography*, *51*(2), 403–418. https://doi.org/10.1175/JPO-D-20-0114.1

Nicholls, K. W. (2018). The study of ice shelf-ocean interaction—Techniques and recent results. *Advances in Polar Science*, *29*(3), 9. https://doi.org/10.13679/j.advps.2018.3.00222

19448007, 2023, 10, Downloaded from https://agupubs.onlinelibrary.wiley.com/doi/10.1029/2023GL102960 by British Antarctic Survey, Wiley Online Library on [15/01/2025]. See the Terms and Conditions (https://onlinelibrary.wiley.com/terms-and-conditions) on Wiley Online Library for rules of use; OA articles are governed by the applicable Creative Commons License